Front. Phys. 13(2), 137303 (2018)
https://doi.org/10.1007/s11467-017-0742-2

RESEARCH ARTICLE

Dynamic conductivity modified by impurity resonant states in doping three-dimensional Dirac semimetals

Shuai Li[1], Chen Wang[2], Shi-Han Zheng[1], Rui-Qiang Wang[1,†], Jun Li[1,‡], Mou Yang[1]

[1] *Guangdong Provincial Key Laboratory of Quantum Engineering and Quantum Materials, School of Physics and Telecommunication Engineering, South China Normal University, Guangzhou 510006, China*
[2] *School of Information Engineering, Guangdong University of Technology, Guangzhou 510006, China*
Corresponding authors. E-mail: †rqwanggz@163.com, ‡lijunc@126.com
Received September 20, 2017; accepted November 28, 2017

The impurity effect is studied in three-dimensional Dirac semimetals in the framework of a T-matrix method to consider the multiple scattering events of Dirac electrons off impurities. It has been found that a strong impurity potential can significantly restructure the energy dispersion and the density of states of Dirac electrons. An impurity-induced resonant state emerges and significantly modifies the pristine optical response. It is shown that the impurity state disturbs the common longitudinal optical conductivity by creating either an optical conductivity peak or double absorption jumps, depending on the relative position of the impurity band and the Fermi level. More importantly, these conductivity features appear in the forbidden region between the Drude and interband transition, completely or partially filling the Pauli block region of optical response. The underlying physics is that the appearance of resonance states as well as the broadening of the bands leads to a more complicated selection rule for the optical transitions, making it possible to excite new electron-hole pairs in the forbidden region. These features in optical conductivity provide valuable information to understand the impurity behaviors in 3D Dirac materials.

Keywords Dirac semimetals, impurity resonance states, optical conductivity

PACS numbers 73.20.-r, 73.63.-b

Frontiers of Physics

1 Introduction

Three-dimensional (3D) Dirac materials, as new topological states of matter extended from 2D Dirac materials such as graphene and topological insulators, are drawing great interest in condensed-matter physics. Experiments have identified a class of materials, for example Cd_3As_2 [1], and Na_3Bi [2], to be Dirac semimetals(DSMs). The DSMs are the bulk analog of graphene and possess degenerate Dirac cones in the spectrum around which topologically protected 3D massless Dirac fermions can be excited [3, 4]. Owing to their topological properties, the band structure is inherently insensitive to weak perturbations [5] and thus Dirac materials are good candidates for electronic devices and quantum computing.

Optical conductivity has been extensively studied as a powerful tool to provide insights into Dirac band dispersion or to probe the transport properties of new topological materials [6–10]. Although various Dirac materials share the same linear energy dispersion, the resulting optical conductivity exhibits diverse features. For graphene [11, 12], one of the most studied 2D Dirac materials, the optical conductivity after the interband onset at twice the value of the chemical potential $2|\mu_F|$ is a constant $e^2/(2h)$, independent of photon energy, which have been confirmed by several experiments [13–15]. Instead, the inter-band optical conductivity for 3D DSMs [16] is in a linear relation to photon energy, which is in general considered as a "smoking gun" for 3D Dirac materials [6, 8] to be uniquely identified from other phases. Breaking either time-reversal symmetry or inversion symmetry will drive the DSMs into a Weyl semimetal (WSM) phase, which is manifested as the splitting of a pair of degenerate Weyl nodes with opposite chirality in momentum or energy space [17, 18]. Interestingly, in optical response, a double-step structure is presented as a unique feature of inversion symmetry breaking Weyl materials. For example, for the WSM TaAs [19], the optical response was found to have a linear dependence below 30 meV, followed by a second linear region between 30 meV and 125 meV with a lower slope, as compared with the first

region.

In realistic materials, impurities or defections are always inevitably introduced and they play an important role in the electron structure of materials. In the studies mentioned above, the optical conductivity is concentrated on the clean Dirac materials. To enable experimental comparison, the impurity effect in Dirac materials needs to be taken into account, where the impurities are commonly modeled as different types of scattering potentials [9, 16]. It has been reported that a constant scattering potential will smear out the steplike structure in the interband optical conductivity, while a scattering proportional to the density of states will modify the slope of the interband background [16]. These studies focused mainly on the case of a weak scattering potential, where the resulting self-energy can be treated with a Born approximation. However, for a strong scattering potential, a full T-matrix approach is required [20]. Importantly, the strong scattering potential can heavily disrupt the pristine Dirac spectrum by generating low-energy resonance states in Weyl semimetals [21, 22] or in topological insulators [23–25] which were also regarded as a mechanism to fill the energy gap created by magnetic impurities [26, 27]. Nevertheless, though there are many reports on the effect of impurity-induced resonance states on the Dirac spectrum [21–31], none of them discussed the resonance-related electrical and optical transport properties. Very recently, we have studied their effect on optical and thermoelectric properties on the doped surface of topological insulators [32] and found that the resonant state leads to interesting phenomena, e.g., reversing the sign of the thermopower. Here, we want to extend the study to doped 3D Dirac materials.

In this paper, we employ a T-matrix method to address the impurity-induced resonant states in band structure and the resulting optical response. It has been found that the impurities significantly disturb the common longitudinal optical conductivity by creating either an optical conductivity peak or new absorption jump, depending on the relative position of the impurity band and the Fermi level. We discuss in detail how the resonance states restructure the electronic dispersion and form new transition channels. In Section 2, we exhibit the impurity-induced self-energy and the impurity state in the framework of a T-matrix method. In Section 3, by performing a Kubo formalism, we calculate the optical conductivities and further discuss the different scenarios and the impact of vertex correction. Finally, a brief summary is given in Section 4.

2 Impurity state in energy spectrum

Before a discussion of dynamic conductance affected by impurity states, we first discuss the formation of impurity states in an energy spectrum. The DSM is described by the minimal Hamiltonian,

$$\hat{H}_0 = \sum_{\boldsymbol{k}} c^{\dagger}_{\boldsymbol{k}}(\hbar v_F \boldsymbol{k}\cdot\boldsymbol{\sigma})c_{\boldsymbol{k}}, \tag{1}$$

where $c^{\dagger}_{\boldsymbol{k}} = (c^{\dagger}_{\boldsymbol{k},\uparrow}, c^{\dagger}_{\boldsymbol{k},\downarrow})$ represents the electron creation operator with momentum $\boldsymbol{k} = (k_x, k_y, k_z)$, and $\boldsymbol{\sigma} = (\sigma_x, \sigma_y, \sigma_z)$ denotes the vector of Pauli matrices for electron spins. The DSM Hamiltonian provides a simple linear energy dispersion $\varepsilon_{\boldsymbol{k}\gamma} = \gamma\hbar v_F|\boldsymbol{k}|$ with $\gamma = \pm$ standing for electron and hole bands, respectively. The bare Green's function of $\hat{H}_0$ is $G_0(\boldsymbol{k}, \mathrm{i}\omega) = [\mathrm{i}\omega - \hat{H}_0]^{-1}$. We are interested in how this pristine dispersion is changed when the DSM bulk is doped. We consider the point-like potential impurities randomly distributed at the position $\boldsymbol{r}_m$ in the form of $V_{im}(\boldsymbol{r}) = \sum_m U\delta(\boldsymbol{r} - \boldsymbol{r}_m)\sigma_0$, where σ_0 is the identity matrix and U is the potential strength. The impurity effect is taken into account by modifying the self-energy of DSM Green's function with a Dyson equation:

$$G(\boldsymbol{k}, \mathrm{i}\omega) = G_0(\boldsymbol{k}, \mathrm{i}\omega)[\sigma_0 - \Sigma(\mathrm{i}\omega)G_0(\boldsymbol{k}, \mathrm{i}\omega)]^{-1}. \tag{2}$$

In leading order approximation which is extensively applied in Dirac materials [33, 34], the impurity induced self-energy takes the form of

$$\Sigma(\mathrm{i}\omega) = n_i U^2 g_0(\mathrm{i}\omega), \tag{3}$$

where $g_0(\mathrm{i}\omega) = \sum_{\boldsymbol{k}} G_0(\boldsymbol{k}, \mathrm{i}\omega)$ and n_i is the impurity concentration. Proceeding with the calculation, we obtain

$$g_0(\omega) = \frac{-1}{4\pi^2(\hbar v_F)^3}\left[2D_c\omega + \omega^2 \ln\left|\frac{D_c - \omega}{D_c + \omega}\right| + \mathrm{i}\pi\omega^2\Theta(D_c - |\omega|)\right], \tag{4}$$

where $\Theta(x)$ is a unitstep function and D_c is the cutoff energy for the bandwidth. Notice that the self-energy in Eq. (3) is a consequence of performing the impurity average over a random distribution, only suitable for weak impurity scattering potential. For stronger potential, one should employ the T-matrix approach [20, 23, 25, 26]

$$\Sigma(\mathrm{i}\omega) = n_i[1 - U g_0(\mathrm{i}\omega)]^{-1}U. \tag{5}$$

Beyond the simple treatment in Eq. (3), this approach considers the multiple local scattering events of an electron around a certain impurity but neglects the correlation between impurities, suitable for the diluted doping with strong scattering potential. In fact, Eq. (3) is equivalent to the first-order approximation of Eq. (5). Here, we employ the T-matrix approach to explore the impurity effect in Dirac semimetals. Substituting Eq. (5) to Eq. (2), one can write the impurity-dressed Green's function as

$$G(\boldsymbol{k}, \mathrm{i}\omega) = \frac{[\mathrm{i}\omega - \Sigma(\mathrm{i}\omega)]\sigma_0 + \hbar v_F \boldsymbol{k}\cdot\boldsymbol{\sigma}}{[\mathrm{i}\omega - \Sigma(\mathrm{i}\omega)]^2 - (\hbar v_F \boldsymbol{k})^2}. \tag{6}$$

Using this, the spectral function matrix in the spin space is calculated by

$$A(\boldsymbol{k},\omega) = -\frac{1}{\pi}\mathrm{Im}[G(\boldsymbol{k},\omega+\mathrm{i}0^+)], \tag{7}$$

where we have analytically continued from Matsubara to real frequencies with $\mathrm{i}\omega \to \omega + \mathrm{i}0^+$.

The numerical results for the spectral function $\mathrm{Tr}_\sigma[A(\boldsymbol{k},\omega)]$ as functions of $\boldsymbol{k}$ and ω are plotted in Fig. 1 for different impurity strengths and concentrations. Figures 1(a)–(d) display the evolution of the DSM energy band with the scalar potential U. Without impurity, $U = 0$, as shown in Fig. 1(a), the spectral function is simply a Dirac-delta function with the spectral weight concentrated at $\omega = \pm\hbar v_F|\boldsymbol{k}|$. Obviously, the energy dispersion displays the behavior of a linear Dirac cone. When impurities are introduced, there emerges an interesting impurity band, whose existence is characterized by the flattened and broadened part below the Dirac point. As U is increased gradually, the impurity band moves towards the Dirac point. The impurity band looks like it splits the valence band into two parts, the upper part having two flat tails spreading horizontally in $\boldsymbol{k}$ space and the lower one developing into an arch. The splitting effect becomes visible for the resonance energy $|\omega_r|$ less than a critical energy E^*, which can be estimated according to Ref. [29]: The total number of states within an energy E of the Dirac point is: $N_E = NV\int_{-E}^{E}\rho_{DOS}\mathrm{d}\omega$, where $\rho_{DOS} = \frac{1}{4\pi^2(\hbar v_F)^3}\omega^2$ is the density of the states, N and V are the total number and volume of the lattice sites. Setting $N_{E^*} = n_i N$ equal to the approximate number of resonance states, one can easily find $E^* = \hbar v_F(6\pi^2 n_i/V)^{\frac{1}{3}}$. With the increase of U, except for the formation of an impurity band, the Dirac point in the energy band structure is shifted upwards, leading to a large electron-hole asymmetry. The reason is attributed to a modification of the chemical potential by $\mathrm{Re}[\Sigma(\omega)]$. For a fixed potential strength, we can tune the impurity concentration n_i to enhance the impurity scattering. From Figs. 1 (e)–(h), one can find that n_i can broaden the impurity-band edges but never change the central position of the impurity band. The formation of the impurity band stems completely from the energy dependence of the imaginary part of self-energy $\mathrm{Im}[\Sigma(\omega)]$.

To clarify the formation for the impurity band, we plot $\mathrm{Im}[\Sigma(\omega)]$ in Fig. 2(a) for different impurity potentials. For the undoped case, the self-energy $\Sigma(\omega)$ vanished. As U is added, the most prominent feature for $\mathrm{Im}[\Sigma(\omega)]$ is the energy dependence. With the increase of U, $\mathrm{Im}[\Sigma(\omega)]$ develops a dip which becomes remarkable and quickly moves towards the Dirac point $\omega = 0$. By comparison, the impurity concentration n_i only enhances the dip height but does not move the dip position. By comparing Fig. 1 with Fig. 2, one can find that the central position ω_c of the impurity state corresponds to that of the dip in $\mathrm{Im}[\Sigma(\omega)]$, which is in turn determined by the real part of the denominator of the T matrix, i.e., $\mathrm{Re}[1 - Ug(\omega_c)] = 0$, from which we obtain $\omega_c = -\frac{2\pi^2}{UD_c}$. Obviously, ω_c is inversely proportional to the impurity potential U, regardless of the impurity concentration n_i, that explains the above behaviors. If $U < 0$, the impurity state will still emerge but in a conduction band.

The impurity state also can be clearly seen in the density of states (DOS), defined as $\rho_{\mathrm{DOS}} = -\frac{1}{\pi}\sum_{\boldsymbol{k}}\mathrm{Im}[\mathrm{Tr}[G(\boldsymbol{k},\omega+\mathrm{i}0^+)]] = \sum_{\boldsymbol{k}}\mathrm{Tr}[A(\boldsymbol{k},\omega)]$, which sums the weight of $\mathrm{Tr}[A(\boldsymbol{k},\omega)]$ for all $\boldsymbol{k}$. We plot the cor-

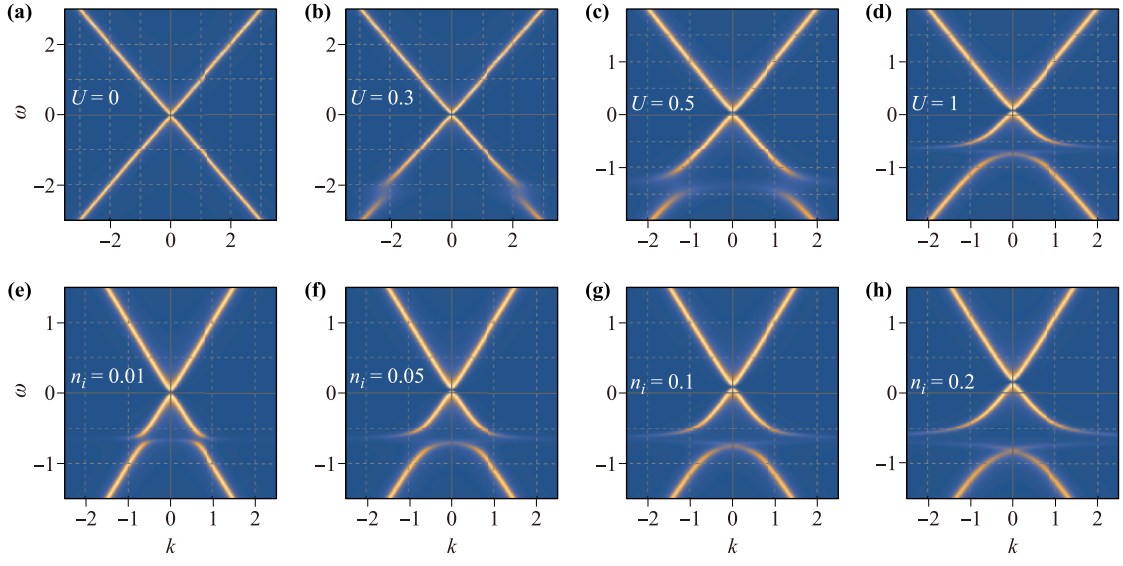

Fig. 1 Evolution of energy dispersion, **(a–d)** for different impurity potentials $U = 0, 0.3, 0.5, 1$ with $n_i = 0.1$, and **(e–h)** for different impurity concentrations $n_i = 0.01, 0.05, 0.1, 0.2$ with $U = 1$. Here $\hbar v_F = 1$ and $D_c = 30$.

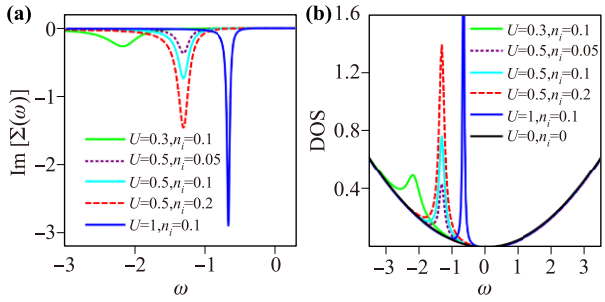

Fig. 2 **(a)** Dependence of the imaginary part of self-energy $\mathrm{Im}[\Sigma(\omega)]$ and **(b)** DOS on potential U and impurity concentration n_i. The other parameters are the same in Fig. 1.

responding DOS as a function of ω in Fig. 2(b), which exhibits a parabola line-shape, different from the linear DOS in the topological insulator [23]. With an increase of U, the impurity band develops into a resonance peak, which becomes sharper and higher when closing to the Dirac point. A larger concentration of impurity will widen the width and increase the peak height of the resonance state. It is apparent that if we adopt the self-energy as defined in Eq. (3), the total DOS is only lifted upward, with no visible impurity band (or resonant state) appearing. This scenario recovers the results when the impurities are modeled as a constant scattering rate [16]. Therefore, it is expected that the presented impurity band will remarkably impact the optical conductivity, beyond the previous studies [9, 16].

3 Optical conductivity

In this section, we will study the influence of the impurity band on the longitudinal optical conductivity by employing the standard procedure of Kubo formula. The current correlation function is defined as $\Pi_{xx}(\mathrm{i}\Omega_n) = -\int_0^{1/(k_BT)} \mathrm{d}\tau \mathrm{e}^{\mathrm{i}\Omega_n\tau}\langle T_\tau j_x^\dagger(\tau) j_x(0)\rangle$, where τ is the imaginary time and T_τ is the time order operator. In the ladder approximation [36], one can write the frequency-dependent correlation function as

$$\Pi_{xx}(\mathrm{i}\Omega_n)=\mathrm{e}^2 k_BT\sum_{\boldsymbol{k},m}\mathrm{Tr}[v_xG(\boldsymbol{k},\mathrm{i}\omega_m)Y_xG(\boldsymbol{k},\mathrm{i}\Omega_n+\mathrm{i}\omega_m)], \tag{8}$$

where T is the temperature, $\omega_m = (2m+1)\pi k_BT$, and the velocity operator is given by $v_x = \partial H_0(\boldsymbol{k})/\partial k_x = \sigma_x$. In Eq. (8), $Y_x = \sigma_x$ if the vertex correction is neglected, then

$$Y_x = \sigma_x + n_iU^2\sum_{\boldsymbol{k}'}\sigma_xG(\boldsymbol{k}',\mathrm{i}\omega_m)Y_xG(\boldsymbol{k}',\mathrm{i}\Omega_n+\mathrm{i}\omega_m), \tag{9}$$

applies to the impurity dressed velocity vertex.

For convenience, we define

$$P(\mathrm{i}\omega_m,\mathrm{i}\Omega_n+\mathrm{i}\omega_m)=\sum_{\boldsymbol{k}}\mathrm{Tr}[\sigma_xG(\boldsymbol{k},\mathrm{i}\omega_m)Y_xG(\boldsymbol{k},\mathrm{i}\Omega_n+\mathrm{i}\omega_m)]. \tag{10}$$

After the summation over a Matsubara frequency $\mathrm{i}\omega_m$, the correlation function reads

$$\begin{aligned}\Pi_{xx}(\mathrm{i}\Omega_n) = -\mathrm{e}^2\int_{-\infty}^{\infty}\frac{\mathrm{d}\omega}{2\pi\mathrm{i}}f(\omega)\times[&P(\omega+\mathrm{i}0^+,\omega+\mathrm{i}\Omega_n)\\ &-P(\omega-\mathrm{i}0^+,\omega+\mathrm{i}\Omega_n)+P(\omega-\mathrm{i}\Omega_n,\omega+\mathrm{i}0^+)\\ &-P(\omega-\mathrm{i}\Omega_n,\omega-\mathrm{i}0^+)],\end{aligned} \tag{11}$$

where $f(\omega) = [\mathrm{e}^{(\omega-\mu_F)/(k_BT)}+1]^{-1}$ is the Fermi distribution function. When one further performs the analytical continuation $\mathrm{i}\Omega_n \to \Omega + \mathrm{i}0^+$ and a variable change $\omega \to \omega + \Omega$ in the last two terms, the imaginary part of the retarded correlation function can be derived as

$$\begin{aligned}\mathrm{Im}[\Pi^r_{xx}(\Omega+\mathrm{i}0^+)] = \mathrm{e}^2\int_{-\infty}^{\infty}\frac{\mathrm{d}\omega}{2\pi}[f(\omega)-f(\omega+\Omega)]&\\ \times\mathrm{Re}[P(\omega-\mathrm{i}0^+,\omega+\Omega+\mathrm{i}0^+)&\\ -P(\omega+\mathrm{i}0^+,\omega+\Omega+\mathrm{i}0^+)],&\end{aligned} \tag{12}$$

where

$$\begin{aligned}P(\omega\mp\mathrm{i}0^+,\omega+\Omega+\mathrm{i}0^+) = \sum_{\boldsymbol{k}}\mathrm{Tr}[\sigma_xG^{A/R}(\boldsymbol{k},\omega)&\\ \times Y_x^{AR/RR}G^R(\boldsymbol{k},\omega+\Omega)],&\end{aligned} \tag{13}$$

with

$$\begin{aligned}Y_x^{AR/RR}=\sigma_x&\\ +n_iU^2\sum_{\boldsymbol{k}'}\sigma_xG^{A/R}(\boldsymbol{k}',\omega)Y_x^{AR/RR}&G^R(\boldsymbol{k}',\omega+\Omega).\end{aligned} \tag{14}$$

The real part of the longitudinal optical conductivity is calculated in terms of the retarded correlation function,

$$\mathrm{Re}\sigma_{xx}(\Omega) = -\frac{1}{\Omega}\mathrm{Im}\{\Pi^r_{xx}(\Omega+\mathrm{i}0^+)\}. \tag{15}$$

With the definition of a spectral function $A(\boldsymbol{k},\omega)$ in Eq. (7), we obtain the final expression for the longitudinal optical conductivity without vertex correction as

$$\begin{aligned}\mathrm{Re}[\sigma_{xx}(\Omega)] = \frac{\mathrm{e}^2\pi}{\Omega}\int_{-\infty}^{\infty}\mathrm{d}\omega[f(\omega)-f(\omega+\Omega)]&\\ \times\sum_{\boldsymbol{k}}\mathrm{Tr}[\sigma_xA(\boldsymbol{k},\omega)\sigma_xA(\boldsymbol{k},\omega+\Omega)].&\end{aligned} \tag{16}$$

The result is identical to the previous formula in Ref. [9], in which it is derived starting from the bubble approximation. Given that the impurity bandhas a significant effect on the spectral function $A(\boldsymbol{k},\omega)$ as discussed in Section 2, it will certainly modify the longitudinal optical conductivity remarkably.

3.1 Influence of impurity states near the Fermi level

Now, we focus on the effect of impurity states on the longitudinal optical conductivity, which is important for understanding the behaviors of impurities. First, we consider the case of the Fermi level near the position ω_c of the impurity band center. In Fig. 3(a), we plot the optical conductivity $\mathrm{Re}\sigma_{xx}$ as a function of the photon energy Ω for different impurity potentials $U = 0, 0.7, 1$, and 1.3, The dotted line denotes the optical conductivity for the clean case ($U = 0$), which exhibits a typical line shape. Around $\Omega = 0$, a sharp Dude peak emerges as a characteristic of a metallic response when the Fermi energy crosses a band, which is a consequence of intraband transitions. At $\Omega = 2|\mu_F|$, an absorption jump of the optical conductivity is presented, which arises from the interband transitions from valence to conduction bands, as indicated by the red arrow in Fig. 3(b). After the onset of the interband absorption, $\mathrm{Re}\sigma_{xx}$ exhibits a linear increase with Ω. One recalls that in 3D topological insulators [37], a similar scenario appears but with the curve tending to a saturated constant in a high frequency limit $\Omega \to \infty$. Here, the linear increase with Ω is regarded as a typical characteristic of three-dimensional Dirac materials as addressed in Refs. [9, 16]. Between the Drude peak and absorption jump, there appears a Pauli blocked region of the optical response, where the optical conductivity is heavily suppressed due to less electron-hole pair excitations.

As U is introduced, as displayed in Fig. 3(a), the most prominent feature is the appearance of a new optical conductivity peak in the Pauli blocked region, which depends nonmonotonously on the potential U. For a fixed Fermi level μ_F above the impurity-band center ω_c, one can tune U to move ω_c towards μ_F, accompanied by the enhancement in the optical conductivity peak. The optical conductivity peak reaches the maximum for $\omega_c = \mu_F$ (red solid line) and then reduces for $\omega_c > \mu_F$ (blue dashed line). In this process, the enhanced weight of the peak is reached by the significant reduction of the weight of the Drude peak. This impurity-induced optical conductivity peak is interesting, which has never been reported for DSM materials in previous studies. More importantly, the conductivity peak fills the Pauli blocked region of the optical response by directly connecting the contribution from both Drude and interband transitions. Obviously, it stems from new channels of the creation of electron-hole pairs.

To gain insight into the unusual behaviors, we illustrate the schematic diagram of optical transitions in the band structure in Fig. 3(b), where $\omega_c = \mu_F$ is chosen. For finite Ω, there exist two types of optical transitions, namely, the transitions within the impurity band and the interband transitions, respectively denoted by the green and red arrows. A detailed analysis shows that the photon frequency of the optical conductivity peak is just equal to the energy difference between the impurity-band upper and lower edges. This implies that the conductivity peak contributed by the transitions from the impurity-band lower to upper edges is at the same momentum $\boldsymbol{k}$. For $\omega_c = \mu_F$, the low energy peak reaches the maximum mainly due to the generation of perfect electron-hole pairs, leading to the highest optical conductivity. In addition, one can see that for different U, the peak position is almost unchanged. This further verifies that the impurity optical conductivity peak does stem from the transitions of impurity-band edges, whose distance remains unchanged with U as indicated in Figs. 1(b)–(d). Interestingly, the appearance of the impurity conductivity peak smears out the absorption jump to divide the Drude and interband terms since the existence of a flat impurity band extends to the intraband conductivity in the valence band to a finite frequency and then mixes it with the interband transitions. Thus, the impurity flat state fills the Pauli blocked region of the optical response and renders the conductivity below

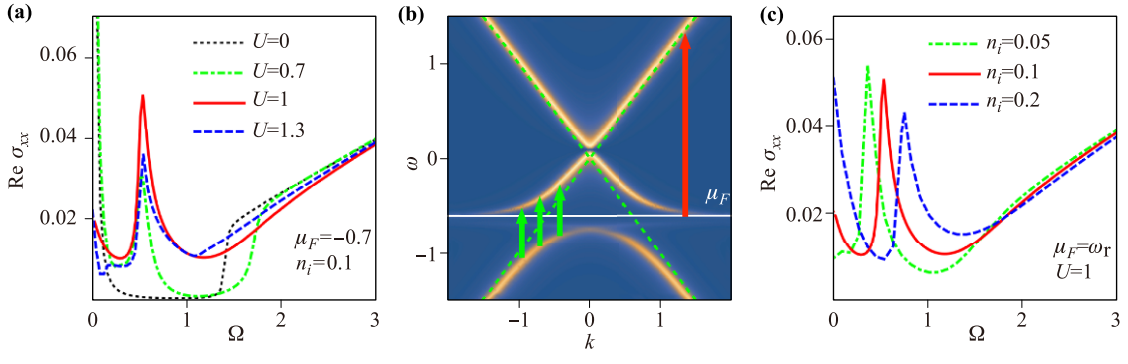

Fig. 3 Optical conductivity of disordered DSM as a function of photon energy Ω for **(a)** different impurity potentials U with a fixed Fermi level $\mu_F = -0.7$ and **(c)** different impurity concentrations n_i with the Fermi level fixed at ω_c. **(b)** Schematic diagram of optical transitions of band structure with $\omega_c = \mu_F$. In (a), the black dotted line is the clean case for comparison. The other parameters are set as $T = 0, \hbar v_F = e = 1$, and $D_c = 30$.

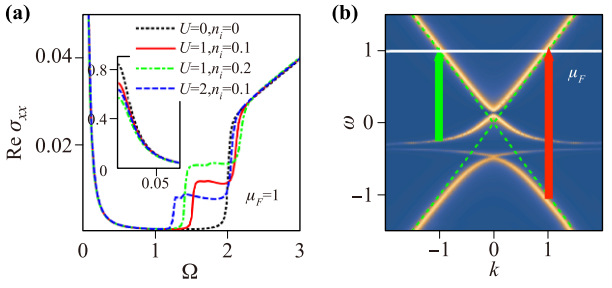

Fig. 4 **(a)** Optical conductivity of disordered Dirac semimetal as a function of photon energy Ω for different potentials U and concentrations n_i with Fermi level far away from resonance states. **(b)** The schematic diagram corresponding to optical transitions. Insert in (a) shows the variation of Drude peak with U and n_i. The other parameters are the same as in Fig. 3.

$2|\mu_F|$ and always finite.

In Fig. 3(c), we demonstrate how the impurity concentration influences the optical conductivity for a fixed $\omega_c = \mu_F$. With the increase of the impurity concentration $n_i = 0.05$, 0.1, and 0.2, the location of the peak shifts to high photon energy. This indicates that the optical transitions from lower to upper edges of the impurity band require more photon energy. The reason is that a strong concentration broadens the width of the impurity band, as depicted in Figs. 1(e)–(h). For $\Omega \to \infty$, all curves tend to approach the same saturated value given by the clean case.

3.2 Influence of impurity states away from the Fermi level

In the following, we shift our focus to presenting the longitudinal optical conductivity $\mathrm{Re}\sigma_{xx}$ for the Fermi level distant from the impurity states. The calculated results are shown in Fig. 4(a) where the black dotted line for $U = 0$ is plotted for reference. From Fig. 4(a), one can see that in the Pauli block region, instead of the conductivity peak, there is a new absorption jump before the onset of the interband transitions. The position of the new jump moves towards the low energy with an increase of U, companied by the reduction of the platform value. This is a consequence of the shifting of the impurity state towards the Dirac point where the DOS is reduced. In order to comprehend the picture, we plot the schematic diagram of optical transitions in Fig. 4(b), where the DSM dispersion seems to split into lower and upper branches according to the impurity resonant state. Two types of main transitions contributing to the optical conductivity are denoted by the green and red arrows. By comparing Figs. 4(a) and (b), it is easy to find that while the high energy jump around $\Omega = 2|\mu_F|$ corresponds to the conventional interband transition, labeled by the red arrow, the new jump is attributed to the flat impurity band-assisted transition denoted by the green arrow. The transition energy between the impurity state and Fermi surface just matches the photon energy at the new jump. Apart from this, the existence of the impurity state also slightly modifies the conventional interband jump at $\Omega = 2|\mu_F|$ due to the valence band deviating from the pristine linear structure. After the step at $2|\mu_F|$, the conductivity still exhibits a linear dependency on photon energy, recovering the undoped case.

In Fig. 4(a) we further compare the curves $n_i = 0.1$ (red solid line) with $n_i = 0.2$ (green dash-dotted line) for $U = 1$. We found that with the increasing impurity concentration n_i, two jumps move respectively to a high and low frequency, due to the broadening of the impurity state as shown in Fig. 1. In the insert of Fig. 4(a), we plot the dependence of the Drude conductivity at the small Ω. With an increase in either impurity strength or concentration, the Drude peak will continually decrease. This is different from the impurity state near the Fermi level as in Fig. 3, where the low-energy peak is due to the intraband transition of the split valence band. Here the low-energy step stems from the interband transition between the newly formed impurity band and the conduction band. However, the common feature is that both of them lift the Pauli block by providing new electron-hole excitation with respect to the impurity band. By contrast, in the previous studies [9, 16], the leading order treatment for impurity could not lead to such a significant effect.

3.3 Vertex correction

In this section, we consider the effect of vertex correction. Following Eq. (9), the vertex function Y_x is easily solved by assuming the common extensive form [38, 39] $Y_x^{AR/RR} = a^{A/R}\sigma_0 + b^{A/R}\sigma_x + c^{A/R}\sigma_y + d^{A/R}\sigma_z$. To determine the parameters, we insert this extensive form into Eq. (9) and arrive at

$$a^{A/R} = c^{A/R} = d^{A/R} = 0,$$
$$b^{A/R} = \frac{1}{1 - \rho U^2 I^{A/R}}, \tag{17}$$

with

$$I^{A/R} = \frac{2}{3}\int \frac{k'^2 \mathrm{d}k'}{(2\pi)^2}\left[\frac{3[\omega - \Sigma^{A/R}(\omega)][\omega + \Omega - \Sigma^{R}(\omega+\Omega)] - k'^2}{\{[\omega - \Sigma^{A/R}(\omega)]^2 - k'^2\}\{[\omega + \Omega - \Sigma^{R}(\omega+\Omega)]^2 - k'^2\}}\right]. \tag{18}$$

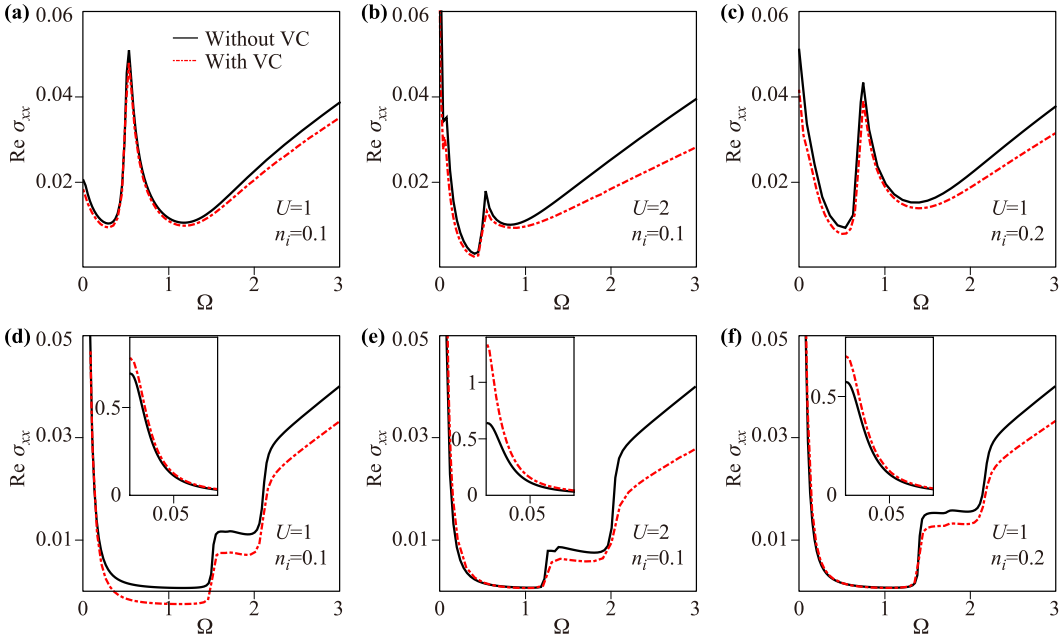

Fig. 5 The vertex correction effect on the optical conductivity of disordered Dirac semimetal for **(a–c)** the impurity band near Fermi level ($\omega_c \approx \mu_F$) and for **(d–f)** the impurity band far away from the Fermi level ($\mu_F = 1$). The black solid lines are the results without vertex correction and the red dashed lines are results with vertex correction. The insets in (d–f) show the variation of the Drude peak. The other parameters are the same in Fig. 3.

Consequently, the vertex correction is $Y_x^{AR/RR} = b^{A/R}\sigma_x$, which reduces to be $Y_x^{AR/RR} = \sigma_x$ in a clean system.

In Fig. 5, we compare the cases with (red dashed lines) and without the vertex correction (black solid lines). The upper panels (a)–(c) are for the impurity band near the Fermi level while the lower panels (d)–(f) are for $|\omega_c - \mu_F| \gg 0$. Whether the impurity band is near or away from the Fermi level, the vertex correction always heavily suppresses the slop in the linear optical conductivity for $\Omega \to \infty$. The suppressed size becomes large with the increase of the impurity potential U and concentration n_i. The reduced weight of interband transitions is transferred to the Drude peak as shown in the inset of panels (d)–(f). By comparison, the upper panels and the lower panels exhibit different responses to the vertex correction in the intermediate region. In Figs. 5(a)–(c) where $\omega_c \approx \mu_F$, the impurity absorption peak is insensitive to the vertex correction while the reduced value of the new plateau in Figs. 5(d)–(f) where $|\omega_c - \mu_F| \gg 0$, is visible due to the vertex correction. Notice that although the vertex correction has an important impact on optical conductivity, it never qualitatively changes the conductivity signature of the impurities.

4 Summary

We have investigated the strong impurity effect on the energy band of 3D Dirac semimetal by employing a T-matrix method and studied the corresponding response in optical conductivity. We determined that a strong impurity potential can induce an impurity resonance state, which significantly restructures the electronic dispersion and DOS spectrum. In turn, the appearance of the impurity resonance state significantly disturbs the longitudinal optical conductivity of clean 3D DSMs by exciting electron-hole pairs in the Pauli block region of optical response. As a consequence, the impurity state manifests itself either as an optical conductivity peak or a new absorption jump of optical conductivity, depending on the relative distance between the impurity band and the Fermi level. Thus, the conventional Pauli block region between the Drude and interband transition is completely or partially lifted, which has never been reported in previous studies. The impurity effect is remarkable for low photon energy and negligible for high photon energy where all optical conductivities tend to attain the same value as that for a clean system, regardless of the impurity parameters. Furthermore, we consider the effect of the vertex correction on the longitudinal optical conductivity. It has been demonstrated that the vertex correction can quantitatively suppress the optical conductivity, but cannot change the conductivity signature of impurities qualitatively. These features in optical conductivity provide important information for understanding the impurity behaviors in 3D Dirac materials.

Acknowledgements This work was supported by Guangdong Province Universities and Colleges Pearl River Scholar Funded Scheme (GDUPS) (2017), the National Natural Science Founda-

tion of China (Grant Nos. 11474106 and 11774100), Guangdong Natural Science Foundation of China (Grant Nos. 2017B030311003 and 2015A030313384), and the Innovation Project of Graduate School of South China Normal University.

References

1. S. Borisenko, Q. Gibson, D. Evtushinsky, V. Zabolotnyy, B. Büchner, and R. J. Cava, Experimental realization of a three-dimensional Dirac semimetal, *Phys. Rev. Lett.* 113(2), 027603 (2014)
2. Z. K. Liu, B. Zhou, Y. Zhang, Z. J. Wang, H. M. Weng, D. Prabhakaran, S. K. Mo, Z. X. Shen, Z. Fang, X. Dai, Z. Hussain, and Y. L. Chen, Discovery of a three-dimensional topological Dirac semimetal Na_3Bi, *Science* 343(6173), 864 (2014)
3. X. C. Pan, Y. M. Pan, J. Jiang, H. K. Zuo, H. M. Liu, X. L. Chen, Z. X. Wei, S. Zhang, Z. H. Wang, X. G. Wan, Z. R. Yang, D. L. Feng, Z. C. Xia, L. Li, F. Q. Song, B. G. Wang, Y. H. Zhang, and G. H. Wang, Carrier balance and linear magnetoresistance in type-II Weyl semimetal WTe_2, *Front. Phys.* 12(3), 127203 (2017)
4. R. Yu, Z. Fang, X. Dai, and H. M. Weng, Topological nodal line semimetals predicted from first-principles calculations, *Front. Phys.* 12(3), 127202 (2017)
5. T. Wehling, A. Black-Schaffer, and A. Balatsky, Dirac materials, *Adv. Phys.* 63(1), 1 (2014)
6. D. Neubauer, J. P. Carbotte, A. A. Nateprov, A. Löhle, M. Dressel, and A. V. Pronin, Interband optical conductivity of the [001]-oriented Dirac semimetalCd_3As_2, *Phys. Rev. B* 93(12), 121202 (2016)
7. Z. G. Chen, R. Y. Chen, R. D. Zhong, J. Schneeloch, C. Zhang, Y. Huang, F. Qu, R. Yu, Q. Li, G. D. Gu, and N. L. Wang, Spectroscopic evidence for bulk-band inversion and three-dimensional massive Dirac fermions in $ZrTe_5$, *Proc. Natl. Acad. Sci. USA* 114(5), 816 (2017)
8. T. Timusk, J. P. Carbotte, C. C. Homes, D. N. Basov, and S. G. Sharapov, Three-dimensional Dirac fermions in quasicrystals as seen via optical conductivity, *Phys. Rev. B* 87(23), 235121 (2013)
9. P. E. C. Ashby, and J. P. Carbotte, Chiral anomaly and optical absorption in Weyl semimetals, *Phys. Rev. B* 89(24), 245121 (2014)
10. C. J. Tabert, and J. P. Carbotte, Optical conductivity of Weyl semimetals and signatures of the gapped semimetal phase transition, *Phys. Rev. B* 93(8), 085442 (2016)
11. V. P. Gusynin, S. G. Sharapov, and J. P. Carbotte, Unusual microwave response of Dirac quasiparticles in graphene, *Phys. Rev. Lett.* 96(25), 256802 (2006)
12. V. P. Gusynin, S. G. Sharapov, and J. P. Carbotte, On the universal ac optical background in graphene, *New J. Phys.* 11(9), 095013 (2009)
13. Z. Q. Li, E. A. Henriksen, Z. Jiang, Z. Hao, M. C. Martin, P. Kim, H. L. Stormer, and D. N. Basov, Dirac charge dynamics in graphene by infrared spectroscopy, *Nat. Phys.* 4(7), 532 (2008)
14. R. R. Nair, P. Blake, A. N. Grigorenko, K. S. Novoselov, T. J. Booth, T. Stauber, N. M. R. Peres, and A. K. Geim, Fine structure constant defines visual transparency of graphene, *Science* 320(5881), 1308 (2008)
15. K. F. Mak, M. Y. Sfeir, Y. Wu, C. H. Lui, J. A. Misewich, and T. F. Heinz, Measurement of the optical conductivity of graphene, *Phys. Rev. Lett.* 101(19), 196405 (2008)
16. C. J. Tabert, J. P. Carbotte, and E. J. Nicol, Optical and transport properties in three-dimensional Dirac and Weyl semimetals, *Phys. Rev. B* 93(8), 085426 (2016)
17. H. Z. Lu and S. Q. Shen, Quantum transport in topological semimetals under magnetic fields, *Front. Phys.* 12(3), 127201 (2017)
18. Y. P. Li, Z. Wang, P. S. Li, X. J. Yang, Z. X. Shen, F. Sheng, X. D. Li, Y. H. Lu, Y. Zheng, and Z. A. Xu, Negative magnetoresistance in Weyl semimetals NbAs and NbP: Intrinsic chiral anomaly and extrinsic effects, *Front. Phys.* 12(3), 127205 (2017)
19. B. Xu, Y. M. Dai, L. X. Zhao, K. Wang, R. Yang, W. Zhang, J. Y. Liu, H. Xiao, G. F. Chen, A. J. Taylor, D. A. Yarotski, R. P. Prasankumar, and X. G. Qiu, Optical spectroscopy of the Weyl semimetal TaAs, *Phys. Rev. B* 93(12), 121110 (2016)
20. A. V. Balatsky, I. Vekhter, and J. X. Zhu, Impurity-induced states in conventional and unconventional superconductors, *Rev. Mod. Phys.* 78(2), 373 (2006)
21. Z. H. Huang, D. P. Arovas, and A. V. Balatsky, Impurity scattering in Weyl semimetals and their stability classification, *New J. Phys.* 15(12), 123019 (2013)
22. S. H. Zheng, R. Q. Wang, M. Zhong, and H. J. Duan, Resonance states and beating pattern induced by quantum impurity scattering in Weyl/Dirac semimetals, *Sci. Rep.* 6(1), 36106 (2016)
23. R. R. Biswas and A. V. Balatsky, Impurity-induced states on the surface of three-dimensional topological insulators, *Phys. Rev. B* 81(23), 233405 (2010)
24. S. H. Zheng, M. X. Deng, J. M. Qiu, Q. H. Zhong, M. Yang, and R. Q. Wang, Interplay of quantum impurities and topological surface modes, *Phys. Lett. A* 379(43), 2890 (2015)
25. R. Q. Wang, L. Sheng, M. Yang, B. Wang, and D. Y. Xing, Electrically tunable Dirac-point resonance induced by a nanomagnet absorbed on the topological insulator surface, *Phys. Rev. B* 91(24), 245409 (2015)
26. A. M. Black-Schaffer, A. V. Balatsky, and J. Fransson, Filling of magnetic-impurity-induced gap in topological insulators by potential scattering, *Phys. Rev. B* 91(20), 201411 (2015)

27. R. Q. Wang, S. H. Zheng, and M. Yang, A new self-filling mechanism of band gap in magnetically doped topological surface states: Spin-flipping inelastic scattering, *New J. Phys.* 18(9), 093048 (2016)
28. Z. Alpichshev, R. R. Biswas, A. V. Balatsky, J. G. Analytis, J. H. Chu, I. R. Fisher, and A. Kapitulnik, STM imaging of impurity resonances on Bi_2Se_3, *Phys. Rev. Lett.* 108(20), 206402 (2012)
29. Y. Xu, J. Chiu, L. Miao, H. He, Z. Alpichshev, A. Kapitulnik, R. R. Biswas, and L. A. Wray, Disorder enabled band structure engineering of a topological insulator surface, *Nat. Commun.* 8, 14081 (2017)
30. M. X. Deng, W. Luo, W. Y. Deng, M. N. Chen, L. Sheng, and D. Y. Xing, Competing effects of magnetic impurities in the anomalous Hall effect on the surface of a topological insulator, *Phys. Rev. B* 94(23), 235116 (2016)
31. M. L. Teague, H. Chu, F. X. Xiu, L. He, K. L. Wang, and N. C. Yeh, Observation of Fermi-energy dependent unitary impurity resonances in a strong topological insulator Bi_2Se_3 with scanning tunneling spectroscopy, *Solid State Commun.* 152(9), 747 (2012)
32. M. Zhong, S. Li, H. J. Duan, L. B. Hu, M. Yang, and R. Q. Wang, Effect of impurity resonant states on optical and thermoelectric properties on the surface of a topological insulator, *Sci. Rep.* 7(1), 3971 (2017)
33. E. V. Gorbar, V. A. Miransky, I. A. Shovkovy, and P. O. Sukhachov, Origin of dissipative Fermi arc transport in Weyl semimetals, *Phys. Rev. B* 93(23), 235127 (2016)
34. H. Z. Lu, S. B. Zhang, and S. Q. Shen, High-field magnetoconductivity of topological semimetals with short range potential, *Phys. Rev. B* 92(4), 045203 (2015)
35. N. M. R. Peres, F. Guinea, and A. H. Castro Neto, Electronic properties of disordered two-dimensional carbon, *Phys. Rev. B* 73(12), 125411 (2006)
36. G. D. Mahan, Many-Particle Physics, 3rd Ed., Plenum, 1993
37. F. Parhizgar, A. G. Moghaddam, and R. Asgari, Optical response and activity of ultrathin films of topological insulators, *Phys. Rev. B* 92(4), 045429 (2015)
38. N. A. Sinitsyn, J. E. Hill, H. Min, J. Sinova, and A. H. MacDonald, Charge and spin Hall conductivity in metallic graphene, *Phys. Rev. Lett.* 97(10), 106804 (2006)
39. V. P. Gusynin, S. G. Sharapov, and A. A. Varlamov, Spin Nernst effect and intrinsic magnetization in two-dimensional Dirac materials, *Low Temp. Phys.* 41(5), 342 (2015)